Modular Assembly and Real-Time Hardware Emulation of On-the-Move Multidomain Multimachine System on More-Electric Aircraft

Zhen Huang , *Student Member, IEEE*, Tong Duan , *Student Member, IEEE*, Chengcheng Tang , *Student Member, IEEE*, and Venkata Dinavahi , *Fellow, IEEE*

***Abstract*—Multi-domain and multi-machine are two significant features of the on-the-move powertrains on more electric aircraft (MEA). To successfully simulate the dynamic behaviors of MEA, not only should the multidisciplinary characteristics be incorporated, but their interfacing issue should be considered. This article presents a modular assembly methodology to model the multi-domain multi-machine system on MEA and achieves real-time emulation on field programmable gate array (FPGA) hardware. The various domain (pneumatic, hydraulic, and mechanical) parts are viewed as modules and interfaced with the electrical domain through machine drive system. State-space model of the power electronic based multi-machine drive system is developed accordingly and the eigenvalue distribution is analyzed. This article also derives practical bounds on real and imaginary part of the eigenvalues to facilitate parallel computation. An 100-machine drive system is then constructed and a Monte Carlo test is performed to validate the effectiveness of the eigenvalue bounds. High fidelity real-time emulation of the MEA multi-domain multi-machine is realized on FPGA. Pneumatic, hydraulic, and mechanical domain characteristics along with the related electrical domain waveforms are exhibited and their comparisons with MATLAB/Simulink are provided. High agreement on these transients waveforms suggests that this modular assembly approach could be a helpful scheme for the modeling and design of MEA powertrains.**

***Index Terms*—Circuit simulation, eigenvalues and eigenfunctions, electrohydraulics, electromechanical effects, parallel processing, pneumatic systems, real-time systems.**

I. INTRODUCTION

MODELING and emulation, especially real-time hardware emulation of the on-the-move electrical powertrains on more electric aircraft poses challenge to most emulation tools
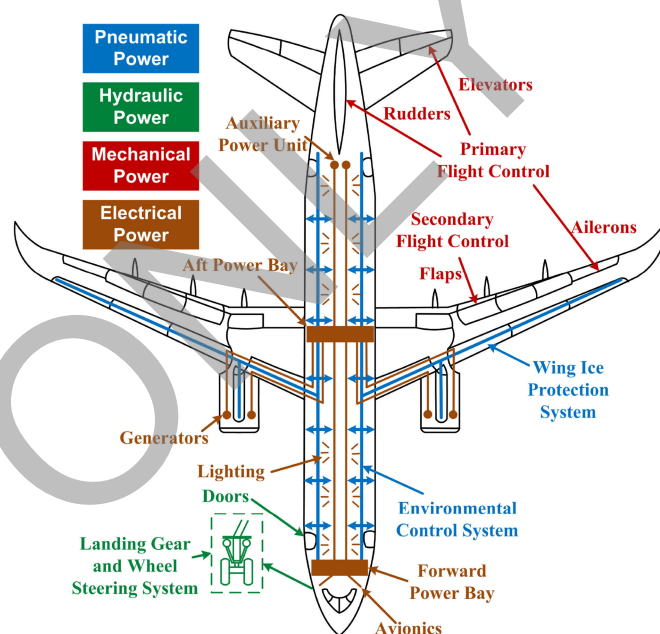
Fig. 1. Power types on aircraft and their typical applications.

due to its high complexity. There are two significant features for the onboard powertrains on more electric aircraft (MEA) that makes this task especially cumbersome, which are multi-domain and multi-machine, respectively.

An aircraft typically needs four types of power in operation, i.e., pneumatic, hydraulic, mechanical, and electrical power, as shown in Fig. 1. Pneumatic system on an aircraft includes the environmental control system (ECS) and the wing ice protection system (WIPS).

Hydraulic implementation include the actuation of steering and extension/retraction system.

Mechanical power can be found in the flight control systems, etc. Electrical energy is overwhelming in low to medium power applications such as avionics, onboard lighting, and entertainment systems. The MEA, as its name implies, aims at replacing as any parts of the pneumatic, hydraulic, and mechanical system with electrical system, which inevitably links different domain techniques together. A high fidelity model should be able to exhibit multidisciplinary characteristics of MEA. That

requirement makes multi-domain an indispensable feature for MEA simulation model.

There are abundant literature modeling one or two domain aspects of MEA parts. However, the comprehensive modeling incorporating all four domain characteristics in one integral model still remains relatively rare in literature because such work does not only require extensive background knowledge from different disciplines, but also needs specially designed cross-domain interfacing scheme. For example, some researches like [1] and [2] mainly focus on the electrical part modeling of MEA while the other domain parts are only represented by very simple structures. Others, on the contrary, have sophisticated models in pneumatic, hydraulic, or mechanical, aspects, but use averaged approach for electrical system modeling, such as the work in [3] and [4]. There are also endeavors like [5] and [6] trying to keep high fidelity on all physical domain models, but various simulation tools like MATLAB/Simulink and Dymola have to be utilized simultaneously. Thus lots of efforts have to be made on cross-platform communication and synchronization.

Modular assembly is deemed an effective strategy to cope with the modeling of multi-domain system. It is believed that the pneumatic, hydraulic, and mechanical parts are linked only through the electrical system and there is no direct influence between them. That is because MEA is designed under the power-by-wire (PBW) principle, i.e., all energy except the propulsion, is transformed into electrical power first and is distributed to different parts by power wires. As a consequence, this complex architecture can be divided into several modules where each module contains only one specific domain and electrical domain model. The challenge then falls on how to correctly assemble these modules into one integral model in the electrical domain. This leads to another important feature of MEA onboard powertrains, that is multi-machine.

Simulation of machines is an intensively studied topic and a widely accepted general-purpose model for single machine is available for use [7]. The difficulty lies on how to interface it with external network. Some programs like PSCAD/EMTDC treat machines as controlled current sources, but such representation introduces one time-step delay regarding the interaction effects between machine and external network. Therefore, additional modifications like added characteristic impedance and compensation are needed to alleviate, not eliminate, its inherent defect. [8] and [9] employ state-space method and eigenvalue locations to analyze the multi-machine system, but no power electronic detail is considered in the system. [10] and [11] use dynamic phasor method to deal with the multi-generator system, but again this method is unable to take into account the effects of switching behavior from power electronic converters because of its averaging approximation during one switching period. More importantly, the machines in these papers are always connected by long distance transmission lines, which is not the case on MEA. Thus, they can not be utilized to solve MEA multi-machine system directly.

[12] made a comprehensive survey on the interfacing techniques that can be utilized to integrate the electrical machines with the rest of power system network. They can be classified into indirect approaches that fit for modified nodal analysis method and direct approaches that fit for state-space method. Indirect approaches are those that interface machine using some post-transformed forms. Generally speaking, they always try to keep a constant admittance matrix to avoid extra computation burden. However, the machine is essentially a time-varying model and modifications like prediction and compensation have to be made. Those modifications always come with detrimental effects on accuracy and numerical stability of the model. Direct approaches, on the other hand, integrate the machine and external network equations together to achieve simultaneous solution of the whole network, thus bringing no extra accuracy and numerical stability loss.

This article aims at achieving real-time emulation of the multi-domain multi-machine system on MEA.

In specific, multiple power electronic based machine drive modules connected by a common DC bus and actuating different domain loads are considered. Because computational efficiency is a crucial factor when choosing emulation scheme, the indirect approaches do not suffice not only because of their side effects on accuracy and numerical stability, but also the fact that even though the admittance matrices of the machines can be made constant, it is a tough task to do so for power electronic converters.

Therefore, direct approach is the selected modeling scheme. In order to realize the modular assembly conception, multiple domain load characteristics and eigenvalue variation along with module number are analyzed. Hardware implementation on FPGA is accomplished for parallel computation and real-time emulation of the multi-domain multi-machine system.

II. Modular Multi-domain Modeling of MEA

The MEA onboard powertrain is a high complexity multi-domain system that it is very cumbersome to model it as a whole. The divide and conquer manner could be a feasible solution wherein the whole system is partitioned into several sub-modules and each module is only responsible for modeling the relationship of one specific domain with electrical domain. There can be multiple instances of the same module but due to the fact that they are linked only through electrical domain and the transients in pneumatic, hydraulic, and mechanical systems are much slower than those in electrical system, it is reasonable to leave the assembly task only in electrical domain, which will be addressed in later sections.

This section describes the multi-domain models used to exhibit in this real-time emulation so that they can be reproduced or embedded into other simulation platforms. It is to be noted that the mathematic description of these models come from various literatures [13]–[23] and are properly transformed into forms that are suitable for interfacing with the state-space model of electrical system in later sections.

A. Electrically Driven Environmental Control System (E-ECS)

As the aircraft engines have become more sensitive to the extraction of bleed air [13], the E-ECS which intakes ambient air as input reaps energy savings over using engine bleed air
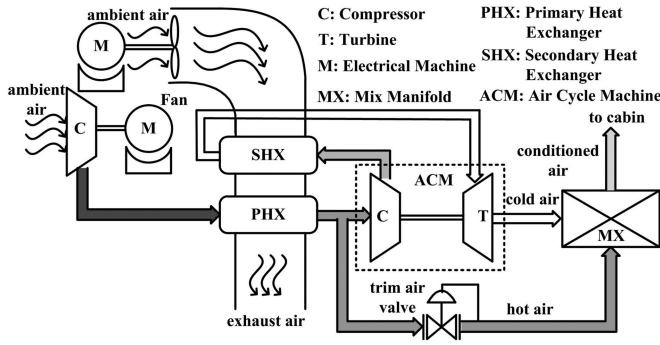
Fig. 2. Schematic of a typical electrically driven ECS.

as it does not require a pressure reduction valve and, as the temperature of the pre-compressor is less than engine bleed air, thus requiring less pre-cooling [14].

A simplified schematic diagram of electrically-driven ECS is shown in Fig. 2 where some advanced features such as humidity control, ozone remover are omitted.

The main parts of E-ECS include compressor and turbine, electrical machine, fan, heat exchanger, and mix manifold. The inlet of E-ECS is actuated by electrical machine and it intakes the ambient air for two purposes: providing cooling flow for heat exchanger and generating pneumatic power (high temperature pressurized air) to air cycle machine (ACM) for post-processing. Noting that the temperature and pressure of ambient air are functions of aircraft altitude, thus the required electrical power also changes along with aircraft mission profile (climb, cruise, descending, etc.)

The pneumatic part of E-ECS operates as an inverse Brayton cycle and can be described by the following equations [15], [16].

1) *Compressor and Fan*

$$P_{\text{out}} = \text{PR} \cdot P_{\text{in}}$$

$$T_{\text{out}} = T_{\text{in}} + \frac{T_{\text{in}}}{\eta_c} \Big(\text{PR}^{(\frac{\gamma-1}{\gamma})} - 1 \Big)$$

$$\text{SP} = \dot{m} \cdot C_p \cdot (T_{\text{out}} - T_{\text{in}}) \tag{1}$$

where P_{in}, T_{in} and P_{out}, T_{out} are input, output pressure and temperature, respectively. PR is pressure ratio. $\dot{m}$ is mass flow rate and SP is shaft power. η_c, γ and C_p are constants referred as compressor/fan efficiency, air heat ratio and air heat capacity, respectively.

2) *Turbine*

$$T_{\text{out}} = T_{\text{in}} - \frac{\text{SP}}{\dot{m}C_p}$$

$$P_{\text{out}} = P_{\text{in}} \left(1 - \frac{T_{\text{in}} - T_{\text{out}}}{\eta_t T_{\text{in}}} \right)^{\frac{\gamma}{\gamma-1}} \tag{2}$$

where η_t is turbine efficiency. All other variables have the same meaning as in (1). Noting that the turbine receives power from the shaft, called compressor-turbine matching, thus the shaft power comes from the compressor on the same shaft.

3) *Heat Exchanger and Mixer Manifold*

$$T_{\text{out}} = \frac{\dot{m}_c \cdot T_c + \dot{m}_h \cdot T_h}{\dot{m}_c + \dot{m}_h}$$

$$P_{\text{hx}} = (1 - \epsilon_{\text{hx}}) \cdot P_{\text{in}}$$

$$P_{\text{mx}} = \frac{\dot{m}_c \cdot P_c + \dot{m}_h \cdot P_h}{\dot{m}_c + \dot{m}_h} \tag{3}$$

where $\dot{m}_c$, T_c and $\dot{m}_h$, T_h are mass flow rate and temperature of the cold and hot air, respectively. The output pressure of heat exchanger and mix manifold are determined by the second and third equation in (3), respectively where ϵ_{hx} is the pressure drop coefficient of heat exchanger.

The cabin temperature based on thermal balance is derived from the First Law of Thermodynamics, which is expressed as:

$$\frac{dT_{\text{cab}}}{dt} = \frac{q_{\text{mx}} + q_s + q_p + q_{\text{fu}}}{C_p \cdot \frac{P_{\text{cab}} \cdot V_{\text{cab}}}{T_{\text{cab}} \cdot R}}$$

$$q_{\text{mx}} = \dot{m}_{\text{mx}} C_p (T_{\text{mx}} - T_{\text{cab}})$$

$$q_s = \phi \cdot \sigma_{\text{fs}} \cdot A_{\text{fs}}$$

$$q_p = q_{\text{pp}} \cdot N_p$$

$$q_{\text{fu}} = \mu (T_{\text{cab}} - T_{\text{amb}}) \tag{4}$$

where T_{cab}, P_{cab}, and V_{cab} are cabin temperature, pressure and volume, respectively. R is the dry air gas constant. q_{mx} is the heat load introduced by E-ECS, i.e., the output of mix manifold. q_s is the heat load generated by solar radiation, which is the product of solar radiation index ϕ ($0 < \phi < 1$), solar radiation intensity σ_{fs} and fuselage area A_{sr}. q_p is the heat load produced by passengers and crew members where q_{pp} is the average heat produced by one person and N_p is the total number of people onboard. q_{fu} represents the heat transfer between the fuselage and the ambient air where μ is the overall fuselage heat conductivity and T_{amb} is the temperature of ambient air.

The cabin temperature is regulated by a trim air valve that controls the hot air entering the mix manifold. When the valve is on, hot air is added to the conditioned air and the raise of q_{mx} will increase T_{cab}. When the valve is off, the q_{mx} drops and results in decrease of T_{cab}. The temperature regulation is achieved by hysteresis control of the difference between the desired and actual temperature in the cabin.

B. Electrohydrostatic Actuator (EHSA)

EHSA combines the benefits of conventional hydraulic systems and direct-drive electrical actuators, namely, high torque/mass ratio and modularity [17], as well as high energy efficiency, due to the fact that the pump works only on a movement demand and the actuating power is transferred by electricity (Power by Wire) instead of by the oil in the pipes (Power by Pipe) [18]. The structure of a typical EHSA is illustrated in Fig. 3. It is composed of an electrical machine as the prime mover, a bidirectional pump regulating the oil flow in the pipes, a safety relief valve for over-pressure protection and a hydraulic cylinder that is split into two chambers to generate force from chamber pressure difference. The bidirectional fixed displacement gear
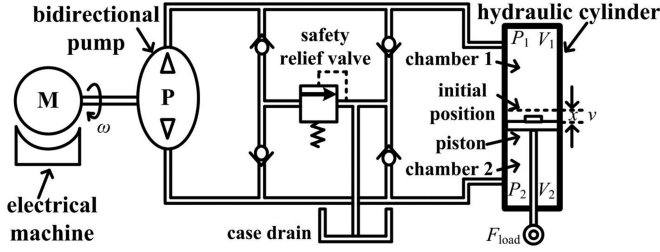
Fig. 3. Schematic of a typical EHSA.

Fig. 4. Schematic of a typical EMA and flight control model.

pump is driven directly by the electrical machine to realize high precision position control and fast system response.

There are one torque balance equation from machine-pump shaft (5), two oil flow continuity equations from each cylinder chamber (6)–(7), one force balance equation (8) and motion equation (9) from piston that are selected to describe the dynamics of EHSA [18], which are outlined as following:

$$J_M \dot{\omega} = T_E - T_P - T_{\text{fr}}(\omega) \tag{5}$$

$$Q_1 = Av + V_1 \dot{P}_1 / \beta + K_{\text{lk}}(P_1 - P_2) \tag{6}$$

$$Q_2 = Av - V_2 \dot{P}_2 / \beta + K_{\text{lk}}(P_1 - P_2) \tag{7}$$

$$A(P_1 - P_2) = m\dot{v} + F_{\text{fr}}(v) + F_{\text{load}} \tag{8}$$

$$\dot{x} = v \tag{9}$$

where J_M is the inertia on machine shaft, ω is the shaft rotating speed, T_E and T_P are electrical torque from machine and hydraulic torque from pump, respectively. $T_{\text{fr}}(\omega)$ is the friction function on the shaft. Q_1, Q_2, P_1, P_2 and V_1, V_2 are the oil flow, pressure and volume in chamber 1 and 2, respectively. A is the area of piston surface, β is the bulk modulus of the oil, K_{lk} is the leakage coefficient of the cylinder. $m, F_{\text{fr}}(v)$ and F_{load} are the total mass, friction force and load force applied on the piston rod. v and x are piston movement velocity and displacement from initial position, respectively.

Apart from the above dynamic equations, each component has its own characteristics equation, which are

$$T_P = D(P_1 - P_2) \tag{10}$$

$$Q_{1,2} = D\omega - K_{\text{lp}}(P_1 - P_2) \tag{11}$$

$$V_1 = V_{10} + Ax \tag{12}$$

$$V_2 = V_{20} - Ax \tag{13}$$

where D is the volumetric pump displacement, K_{lp} is pump leakage coefficient. V_{10} and V_{20} are the initial volume of chamber 1 and 2, respectively.

$T_{\text{fr}}(\omega)$ and $F_{\text{fr}}(v)$ are two functions that use the LuGre model to capture friction phenomenon. The LuGre model contains only a few parameters but has the ability to model viscous friction, coulomb friction as well as Stribeck effect for predicting stick-slip motion, thus it can easily be matched to experimental data [19]. The LuGre model takes the form of (14),

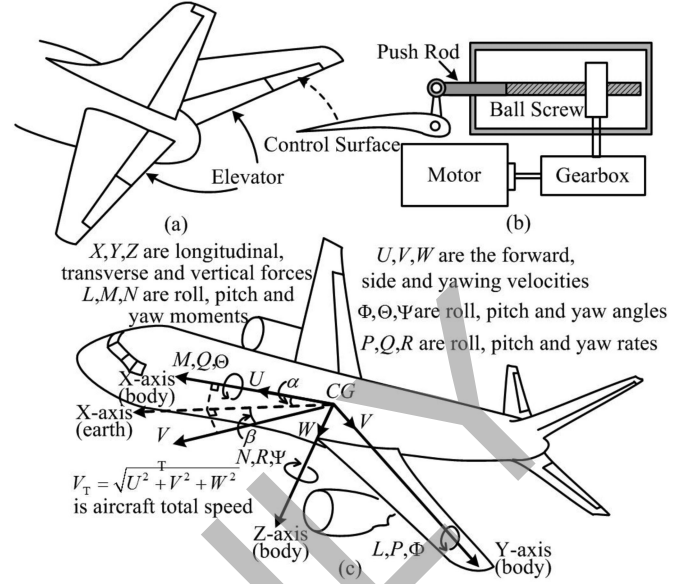$$L_{\text{fr}}(z) = A_c \cdot \text{sgn}(z) + B_c \cdot z + C_c \cdot \text{sgn}(z) e^{-|z/z_c|} \tag{14}$$

where A_c and C_c are two constants corresponding to coulomb friction and stiction friction, respectively. z_c is a parameter determining how fast the stiction friction approaches zero and B_c characterizes the viscous friction. There are only four parameters in the model, so it is convenient for experimental parameter identification.

Combining the derivative equations from (5)–(9) and the component characteristics equations from (10)–(13), the state-space model of the EHSA system can be obtained, which are written as following:

$$\begin{cases} \dot{\omega} = \frac{1}{J_M}(T_E - D(P_1 - P_2) - T_{\text{fr}}(w)) \\ \dot{P}_1 = \frac{\beta}{V_{10} + Ax}(D\omega - K_l(P_1 - P_2) - Av) \\ \dot{P}_2 = \frac{\beta}{V_{20} - Ax}(-D\omega + K_l(P_1 - P_2) + Av) \\ \dot{v} = \frac{1}{M}(A(P_1 - P_2) - F_{fr}(v) - F_{\text{load}}) \\ \dot{x} = v \end{cases} \tag{15}$$

where $K_l = K_{lk} + K_{lp}$ is the combined leakage coefficient.

$T_{\text{fr}}(\omega)$ and $F_{\text{fr}}(v)$ are the major contributors of nonlinearities in the system that have significant effect on the start-up process, which will be demonstrated in later section.

C. Electromechanical Actuator (EMA)

The EMA is an apparatus that leverages on a gearbox and ball screw system to translate rotary motion into linear motion [20]. The aircraft flight control dynamics along with EMA performance is of great interest for MEA designers and engineers. In this section, an EMA serving as elevator for aircraft longitudinal control is selected as representative case-study, as shown in Fig. 4(a) and (b).

The linear motion changes the position of elevator surface and then affects the aircraft body correspondingly. According to [21]–[23], the small-disturbance kinematics equations of aircraft longitudinal motions from an equilibrium state can be

expressed as:

$$
\begin{cases}
m\left(\dot{u} + W_0 q - g\cos\Theta_0\theta\right) \\
\quad = \Delta X = \frac{\partial X}{\partial u}u + \frac{\partial X}{\partial w}w + \frac{\partial X}{\partial \delta_E}\delta_E \\
m\left(\dot{w} - U_0 q + g\sin\Theta_0\theta\right) = \Delta Z \\
\quad = \frac{\partial Z}{\partial u}u + \frac{\partial Z}{\partial w}w + \frac{\partial Z}{\partial \dot{w}}\dot{w} + \frac{\partial Z}{\partial q}q + \frac{\partial Z}{\partial \delta_E}\delta_E \\
I_y\dot{q} = \Delta M = \frac{\partial M}{\partial u}u + \frac{\partial M}{\partial w}w + \frac{\partial M}{\partial \dot{w}}\dot{w} + \frac{\partial M}{\partial q}q + \frac{\partial M}{\partial \delta_E}\delta_E \\
\dot{\theta} = q
\end{cases}
$$

$$(16)$$

where m is aircraft mass, I_y is its y-axis inertia. The meaning of other parameters can be found in Fig. 4(c). The subscript 0 represents the initial value at the selected equilibrium state while the lower case variable and prefix Δ means the small-scale perturbation corresponding to the upper case variables. The deviation of forces and moments ΔX, ΔZ, and ΔM can be expressed as combined contribution of system states $[u, w, q, \theta]$ and input elevator control surface perturbation δ_E. The relevant partial derivatives are aerodynamic coefficients that can be estimated by wind tunnel tests or system identification based on logged experimental data from the aircraft [23]. Some depending terms are omitted because they are generally insignificant, for example $\frac{\partial X}{\partial q}$ is ignored since q has negligible effect on u.

Based on (16), the state-space model of the small-disturbance aircraft longitudinal dynamics can be written in canonical form as follows:

$$
\begin{cases}
\dot{u} = X_u u + X_w w + W_0 q - g\cos\Theta_0\theta + X_{\delta_E}\delta_E \\
\dot{w} = Z_u u + Z_w w + U_0 q - g\sin\Theta_0\theta + Z_{\delta_E}\delta_E \\
\dot{q} = (M_u + M_{\dot{w}}Z_u)u + (M_w + M_{\dot{w}}Z_w)w \\
\quad + (M_q + M_{\dot{w}}U_0)q - M_{\dot{w}}g\sin\Theta_0\theta + M_{\delta_E}\delta_E \\
\dot{\theta} = q
\end{cases}
$$

$$(17)$$

where $[u, w, q, \theta]$ is system state vector, δ_E is input control variable associated with elevator position and the following notations are used:

$$
X_x = \frac{1}{m}\frac{\partial X}{\partial x}, \quad Z_x = \frac{1}{m}\frac{\partial Z}{\partial x}, \quad M_x = \frac{1}{I_y}\frac{\partial M}{\partial x}
$$

where x can be system state or input variable.

III. ASSEMBLY ANALYSIS OF MULTIMACHINE SYSTEM

Once the sub-systems involving the relation of each domain with electrical domain are transformed into modular models, the next task should be assembling them into an integrated system. This section deals with the eigenvalue analysis of power electronic converter based multi-machine drive system so as to provide facility for solving it in real-time using parallel algorithm on FPGA.

Fig. 5(a) depicts the general structure of the multi-machine drive system on MEA. This system is fed by a rippled dc voltage source that is converted from ac bus by auto transformer rectifier unit (ATRU). The rippled dc voltage is smoothed by an LC filter and then feds the dc bus. The multiple machine drive modules are connected in parallel on the dc bus while the other domain systems are linked with the electrical domain system through
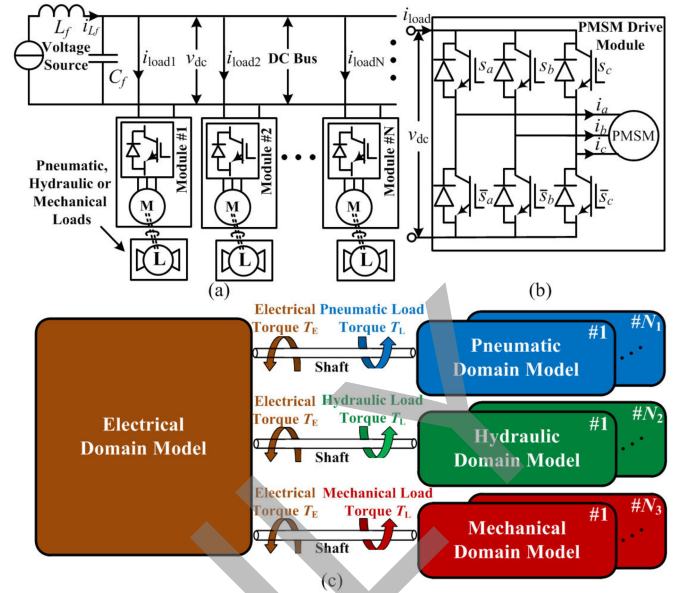

Fig. 5. General structure of the multimachine drive system on MEA.

the machine shaft so that they can be viewed as torque loads applied on the shaft. As can be seen in Fig. 5(c), the shafts are the interfaces connecting pneumatic, hydraulic, and mechanical modules with the electrical system. The electrical torque T_E generated by machines can be obtained through computation of machine currents and flux information while the load torques are calculated from other domain modules. For example, the pneumatic torque from E-ECS is the shaft power SP in (1) divided by shaft angular speed ω; the hydraulic torque from EHSA is the sum of pump and friction torque in (5); the mechanical torque from EMA for flight control is a function of air density, airplane speed and weather, etc. Usually it can be viewed as constant during a small period of time.

The multi-machine drive system is generally regarded as a very complicated structure that high fidelity modeling requires much effort. To simplify the analysis process yet still attain constructive conclusions, the following assumptions are made.

1) The internal impedance of the dc source in the system is deemed negligible or insignificant compared with the LC filter so that it can be viewed as "ideal" source.
2) The transients of the torque loads generated by the pneumatic, hydraulic, and mechanical system are much slower so they have negligible impact on the electrical system transients (eigenvalues).

The above assumptions are generally true except for some extreme cases. It would suffice to yield insightful results in most cases such as performance evaluation, control parameter tunning, etc. It is a good compromise between accuracy and complexity in terms of mathematic modeling.

Before analyzing the eigenvalues of multi-machine drive system, it is necessary to clarify the single machine drive system as the first step. The permanent magnet synchronous machine (PMSM) is viewed as the best suited type for applications on MEA because of its high power density and torque-to-inertia

ratio as well as low losses [24]. Therefore, the three-phase two-level converter PMSM drive system depicted in Fig 5(b) is selected as the module structure for study. A PMSM can be described by the following dq equivalent circuit equations [7]:

$$
\begin{cases}
v_d = r_s i_d - \lambda_q \omega + \dot\lambda_d \\
v_q = r_s i_q + \lambda_d \omega + \dot\lambda_q \\
v_0 = r_s i_0 + \dot\lambda_0 \\
0 = r'_{kd} i'_{kd} + \dot\lambda'_{kd} \\
0 = r'_{kq} i'_{kq} + \dot\lambda'_{kq}
\end{cases}
,
\begin{cases}
\lambda_d = L_d i_d + L_{md} i'_{kd} + \lambda'_m \\
\lambda_q = L_q i_q + L_{mq} i'_{kq} \\
\lambda_0 = L_{ls} i_0 \\
\lambda'_{kd} = L_{md} i_d + L'_{kd} i'_{kd} + \lambda'_m \\
\lambda'_{kq} = L_{mq} i_q + L'_{kq} i'_{kq}
\end{cases}
\tag{18}
$$

where v, λ, L and r represents winding voltage, flux, inductance and resistance, respectively. The subscripts d, q and s denote d, q axis and stator winding parameters, respectively while subscripts k and m denote damper winding and mutual parameters. The superscript $'$ means the parameter is stator side equivalent. λ'_m is the flux induced by permanent magnet and can be viewed as constant. $\omega = \dot\theta$ is electrical angular velocity and is equal to the derivative of electrical rotor angular position θ.

The d and q axis variables and a, b, and c axis variables can be transformed using the well known Park's and inverse Park's transformation, which can be found in [7].

As a result, the dq axis applied voltages and the load current that a machine extracted from the dc bus can be expressed as:

$$
v_d = f_1(\theta, s_a, s_b, s_c) v_{dc}
$$
$$
= \frac{2}{3}\left[\cos(\theta)s_a + \cos\left(\theta - \frac{2}{3}\pi\right)s_b + \cos\left(\theta + \frac{2}{3}\pi\right)s_c\right]v_{dc}
$$
$$
v_q = f_2(\theta, s_a, s_b, s_c) v_{dc}
$$
$$
= -\frac{2}{3}\left[\sin(\theta)s_a + \sin\left(\theta - \frac{2}{3}\pi\right)s_b + \sin\left(\theta + \frac{2}{3}\pi\right)s_c\right]v_{dc}
$$
$$
v_0 = f_3(\theta, s_a, s_b, s_c) v_{dc} = \frac{1}{3}\left(s_a + s_b + s_c\right)v_{dc}
$$
$$
i_{\text{load}} = s_a i_a + s_b i_b + s_c i_c = f_1 i_d + f_2 i_q + f_3 i_0
$$
$$
= f_1 \frac{L'_{kd}\lambda_d - L_{md}\lambda'_{kd} + (L_{md} - L'_{kd})\lambda'_m}{\sigma_d}
$$
$$
+ f_2 \frac{L'_{kq}\lambda_q - L_{mq}\lambda'_{kq}}{\sigma_q} + f_3 \frac{\lambda_0}{L_{ls}}
\tag{19}
$$

where s_a, s_b, and s_c are switching signals of the upper arm switch in each phase. They are either 1 or 0, representing switch on and off state, respectively. $f_1(\theta, s_a, s_b, s_c)$, $f_2(\theta, s_a, s_b, s_c)$ and $f_3(s_a, s_b, s_c)$ (denoted as f_1, f_2, and f_3 henceforth), are three functions of switching signals and rotor position θ, their expressions can be found in (19) and $\sigma_d = L'_{kd}L_d - L_{md}^2$, $\sigma_q = L'_{kq}L_q - L_{mq}^2$.

Combining (18) and (19), the state-space form of single PMSM drive system is derived:

$$
\begin{bmatrix} \dot\lambda \\ \dot v_{dc} \end{bmatrix} = \begin{bmatrix} \mathbf{A}_{11} & \mathbf{A}_{12} \\ \mathbf{A}_{21} & 0 \end{bmatrix} \begin{bmatrix} \lambda \\ v_{dc} \end{bmatrix} + \mathbf{B}\lambda'_m
\tag{20}
$$

where

$$
\boldsymbol\lambda = \begin{bmatrix} \lambda_d \\ \lambda_q \\ \lambda_0 \\ \lambda'_{kd} \\ \lambda'_{kq} \end{bmatrix},
$$

$$
\mathbf{A}_{11} = \begin{bmatrix}
-\frac{r_s L'_{kd}}{\sigma_d} & \omega & 0 & \frac{r_s L_{md}}{\sigma_d} & 0 \\
-\omega & -\frac{r_s L'_{kq}}{\sigma_q} & 0 & 0 & \frac{r_s L_{mq}}{\sigma_q} \\
0 & 0 & -\frac{r_s}{L_{ls}} & 0 & 0 \\
\frac{r'_{kd} L_{md}}{\sigma_d} & 0 & 0 & -\frac{r'_{kd} L_d}{\sigma_d} & 0 \\
0 & \frac{r'_{kq} L_{mq}}{\sigma_q} & 0 & 0 & -\frac{r'_{kq} L_q}{\sigma_q}
\end{bmatrix}
$$

$$
\mathbf{A}_{12} = \begin{bmatrix} f_1 \\ f_2 \\ f_3 \\ 0 \\ 0 \end{bmatrix}, \ \mathbf{A}_{21} = \begin{bmatrix} -\frac{L'_{kd}}{\sigma_d C_f} f_1 \\ -\frac{L'_{kq}}{\sigma_q C_f} f_2 \\ -\frac{1}{L'_{ls} C_f} f_3 \\ \frac{L_{md}}{\sigma_d C_f} f_1 \\ \frac{L_{mq}}{\sigma_q C_f} f_2 \end{bmatrix}^T, \ \mathbf{B} = \begin{bmatrix} -\frac{r_s(L_{md}-L'_{kd})}{\sigma_d} \\ 0 \\ 0 \\ -\frac{r'_{kd}(L_{md}-L_d)}{\sigma_d} \\ 0 \\ -\frac{L_{md}-L'_{kd}}{\sigma_d C_f} f_1 \end{bmatrix}
\tag{21}
$$

and the superscript T means matrix transpose.

Accordingly, the state-space model of the multi-machine drive system linked by a common dc bus can be written as

$$
\begin{bmatrix} \dot{\boldsymbol\lambda}^1 \\ \dot{\boldsymbol\lambda}^2 \\ \vdots \\ \dot{\boldsymbol\lambda}^N \\ \dot v_{dc} \\ \dot i_{L_f} \end{bmatrix} = \underbrace{\begin{bmatrix}
\mathbf{A}_{11}^{(1)} & \mathbf{0} & \cdots & \mathbf{0} & \mathbf{A}_{12}^{(1)} & \mathbf{0} \\
\mathbf{0} & \mathbf{A}_{11}^{(2)} & \cdots & \mathbf{0} & \mathbf{A}_{12}^{(2)} & \mathbf{0} \\
\vdots & \vdots & \ddots & \vdots & \vdots & \vdots \\
\mathbf{0} & \mathbf{0} & \cdots & \mathbf{A}_{11}^{(N)} & \mathbf{A}_{12}^{(N)} & \mathbf{0} \\
\mathbf{A}_{21}^{(1)} & \mathbf{A}_{21}^{(2)} & \cdots & \mathbf{A}_{21}^{(N)} & 0 & \frac{1}{C_f} \\
\mathbf{0} & \mathbf{0} & \cdots & \mathbf{0} & -\frac{1}{L_f} & 0
\end{bmatrix}}_{\mathbf{A}_{(5N+2)\times(5N+2)}} \begin{bmatrix} \boldsymbol\lambda^1 \\ \boldsymbol\lambda^2 \\ \vdots \\ \boldsymbol\lambda^N \\ v_{dc} \\ i_{L_f} \end{bmatrix}
\tag{22}
$$

where the superscript n ($1 \le n \le N$) denotes the nth module state variables in the system. They have the same form and meaning with that in (21). The input matrix $\mathbf{B}$ associated with λ'_m and voltage source are omitted because they have no effect on system eigenvalues.

As can be seen that all the block matrices $\mathbf{A}_{11}^{(k)}$, $\mathbf{A}_{12}^{(k)}$, and $\mathbf{A}_{21}^{(k)}$ are time-varying as different modules may have different angular velocities (ω) and switching states (f_1, f_2, f_3). Therefore, it is not advisable to solve it using some implicit numerical methods like the Trapezoidal method because they need to conduct matrix division or its equivalent at every time-step, thus making the computational complexity grows by $O(N^3)$. On the other hand, the explicit methods only need matrix multiplication and addition during the computation process and these computations can be decomposed into parallel steps, which are very suitable to be implemented on FPGA for real-time emulation purpose.

However, one limitation that explicit methods have in common is the bounded numerical stability region. It is required

that all the eigenvalues of the system times time-step must locate within the stability region. Therefore, ascertaining the system eigenvalue bounds becomes necessary before selecting the appropriate numerical method and time-step.

Since there are infinite variations of $\mathbf{A}$, it is impractical to find all its possible eigenvalues. However, there are some properties of $\mathbf{A}$ that can be leveraged to seek its eigenvalue bounds.

First of all, $\mathbf{A}$ can be decomposed into the sum of two matrices $\mathbf{A} = \mathbf{A_1} + \mathbf{A_2}$, where

$$\mathbf{A}_1 = \begin{bmatrix} \mathbf{A}_{11}^1 & \mathbf{0} & \cdots & \mathbf{0} & \mathbf{0} & \mathbf{0} \\ \mathbf{0} & \mathbf{A}_{11}^2 & \cdots & \mathbf{0} & \mathbf{0} & \mathbf{0} \\ \vdots & \vdots & \ddots & \vdots & \vdots & \vdots \\ \mathbf{0} & \mathbf{0} & \cdots & \mathbf{A}_{11}^N & \mathbf{0} & \mathbf{0} \\ \mathbf{0} & \mathbf{0} & \cdots & \mathbf{0} & 0 & 0 \\ \mathbf{0} & \mathbf{0} & \cdots & \mathbf{0} & 0 & 0 \end{bmatrix},$$

$$\mathbf{A}_2 = \begin{bmatrix} \mathbf{0} & \mathbf{0} & \cdots & \mathbf{0} & \mathbf{A}_{12}^1 & \mathbf{0} \\ \mathbf{0} & \mathbf{0} & \cdots & \mathbf{0} & \mathbf{A}_{12}^2 & \mathbf{0} \\ \vdots & \vdots & \ddots & \vdots & \vdots & \vdots \\ \mathbf{0} & \mathbf{0} & \cdots & \mathbf{0} & \mathbf{A}_{12}^N & \mathbf{0} \\ \mathbf{A}_{21}^1 & \mathbf{A}_{21}^2 & \cdots & \mathbf{0} & 0 & \frac{1}{C_f} \\ \mathbf{0} & \mathbf{0} & \cdots & \mathbf{0} & -\frac{1}{L_f} & 0 \end{bmatrix}.$$

Special attention should be given to $\mathbf{A}_2$ because 1) $\mathbf{A}_2$ has rank of only 2; and 2) $\mathbf{A}_2$ is a bipartite matrix, regardless of how $\mathbf{A}_{12}^{(k)}$ and $\mathbf{A}_{21}^{(k)}$ vary. A matrix $\mathbf{M}_{n \times n}$ is bipartite when it is possible to partition $\{1, 2, \ldots, n\}$ into two sets V_1 and V_2 so that for every $m_{ij} \neq 0$ in $\mathbf{M}$, i and j separately belong to V_1 and V_2 (i.e., i and j will not be in the same set).

It is clear that one feasible partition for $\mathbf{A}_2$ is placing $(5N + 1)$ in V_1 and placing 1 to $(5N + 2)$ except $(5N + 1)$ in V_2. According to [25], if μ is an eigenvalue of a bipartite matrix $\mathbf{M}$ with multiplicity k, then $-\mu$ is also an eigenvalue of $\mathbf{M}$ with multiplicity k. Considering the fact that $\mathbf{A}_2$ has only two nonzero eigenvalues, they must appear in conjugate pairs because $\mathbf{A}_2$ is real and they are opposite numbers because $\mathbf{A}_2$ is bipartite, then there is only one possibility: they are two pure imaginary numbers $\pm j\gamma$. More importantly, $\mathbf{A}_2$ is diagonalizable because the algebraic multiplicity of every eigenvalue equals its geometric multiplicity ($\pm j\gamma$ have multiplicity 1 and eigenvalue 0 has multiplicity $5N$). Therefore, there exists a nonsingular matrix $\mathbf{P}$ so as to make $\mathbf{PA_2P}^{-1}$ a diagonal matrix with its eigenvalues on the diagonal entries. Moreover, it is not prohibitive to conduct the same similarity transformation on $\mathbf{A}$ since it will not change the eigenvalues.

$$\bar{\mathbf{A}} = \mathbf{PAP}^{-1} = \mathbf{PA_1P}^{-1} + \mathbf{PA_2P}^{-1} = \bar{\mathbf{A}}_1 + \bar{\mathbf{A}}_2$$

$$= \mathbf{PA_1P}^{-1} + \begin{bmatrix} j\gamma & 0 & \mathbf{0} \\ 0 & -j\gamma & \mathbf{0} \\ \mathbf{0} & \mathbf{0} & \mathbf{0}_{(5N \times 5N)} \end{bmatrix} \quad (23)$$

where $\bar{\mathbf{A}}_2$ is a diagonal matrix which is similar to $\mathbf{A}_2$.

According to [26], if μ is an eigenvalue of $\mathbf{M}_1 + \mathbf{M}_2$, then $\mu \in F(\mathbf{M}_1) + F(\mathbf{M}_2)$, where $F(\mathbf{M})$ is called the field of values defined as $F(\mathbf{M}) \equiv \{\mathbf{x}^*\mathbf{M}\mathbf{x} \mid \mathbf{x} \text{ is a complex vector and } \mathbf{x}^*\mathbf{x} = 1\}$. Obviously, $F(\bar{\mathbf{A}}_2)$ is a closed interval between $[-j\gamma, j\gamma]$ on the imaginary axis. Then the eigenvalues of $\bar{\mathbf{A}}$ must locate within the union area that $F(\bar{\mathbf{A}}_1)$ move upward and downward along the imaginary-axis (vertically) for a length γ. Hence, the problem comes down to identifying $F(\bar{\mathbf{A}}_1)$ or equivalently, $F(\mathbf{A}_1)$. The following two theorems in [27] and [28] can help:

Theorem 1: If $\mathbf{M} = \mathbf{H}_1 + j\mathbf{H}_2$ with $\alpha_1 \leq \alpha_2 \leq \cdots \leq \alpha_n$ the eigenvalues of $\mathbf{H}_1$ and $\beta_1 \leq \beta_2 \leq \cdots \leq \beta_n$ the eigenvalues of $\mathbf{H}_2$, then the points of $F(\mathbf{M})$ lie in the interior or on the boundary of the rectangle constructed by the lines $\xi = \alpha_1, \xi = \alpha_n; \eta = \beta_1, \eta = \beta_n$ positioned parallel to the axes, where $\mathbf{H}_1$ and $\mathbf{H}_2$ are two hermitian matrices defined as: $\mathbf{H}_1 = (\mathbf{M} + \mathbf{M}^*)/2, \mathbf{H}_2 = (\mathbf{M} - \mathbf{M}^*)/(2j)$.

Theorem 2: Let $\mathbf{M}$ be an $n \times n$ complex matrix with real eigenvalues $\mu(\mathbf{M})$, and let $m = \operatorname{tr}(\mathbf{M})/n, s^2 = \operatorname{tr}(\mathbf{M}^2)/n - m^2$, then $m - s(n-1)^{1/2} \leq \mu(\mathbf{M}) \leq m + s(n-1)^{1/2}$, where tr means trace of the matrix.

Since $\mathbf{A}_1$ is a diagonal block matrix, the eigenvalue identifying can be conducted block-wise and then synthesize. In other words, the max/min eigenvalue of $\mathbf{A}_1$ is the max/min eigenvalue among all its blocks $\mathbf{A}_{11}^{(k)}$. It is worth mentioning that the real part bounds (α_1 and α_n) of $\mathbf{A}_{11}$ are invariant with angular velocity ω. They are determined only by machine electrical parameters (r, L, σ, etc.). While the imaginary part bounds ($\beta_n = -\beta_1 = \beta(\omega)$) are functions of ω:

$$\beta(\omega) = \sqrt{\frac{2}{5}\omega^2 + \frac{1}{10}\left(\frac{r_s - r'_{kd}}{\sigma_d}L_{md}\right)^2 + \frac{1}{10}\left(\frac{r_s - r'_{kq}}{\sigma_q}L_{mq}\right)^2}. \quad (24)$$

The upper bound $\bar{\beta}$ is achieved when ω equals the maximum angular velocity ω_m.

Meanwhile, the imaginary interval of $\mathbf{A}_2$ can be written as

$$\gamma = \sqrt{\sum_{k=1}^N \left(\frac{L'^{(k)}_{kd}}{\sigma_d^{(k)}C_f}f_1^2 + \frac{L'^{(k)}_{kq}}{\sigma_q^{(k)}C_f}f_2^2 + \frac{f_3^2}{L_{ls}^{(k)}C_f}\right) + \frac{1}{L_fC_f}}. \quad (25)$$

Since $f_1, f_2 \in [-\frac{2}{3}, \frac{2}{3}], f_3 \in [0, 1]$, the upper bound $\bar{\gamma}$ is achieved when $f_1 = f_2 = \frac{2}{3}$, and $f_3 = 1$.

To verify the effectiveness of the above eigenvalue bounds, a Monte Carlo test is performed on a multi-machine system that has a total of 100 machines, where the values of angular velocity ω and f_1, f_2, f_3 are given randomly in their range. The corresponding bounds and system eigenvalues in 10 000 tests are demonstrated in Fig. 6. As can be seen that all the eigenvalues are located within the rectangular area constrained by the real and imaginary part bounds.

As an extensible modular model, another meaningful thing is to know how eigenvalue bounds will change when adding or removing one module from the system. Based on the above analysis, it can be concluded that adding or removing one module from the system does not change its real part bounds unless the real parts of the added or removed module's eigenvalues exceed the remaining system's real part bounds. However, it will always
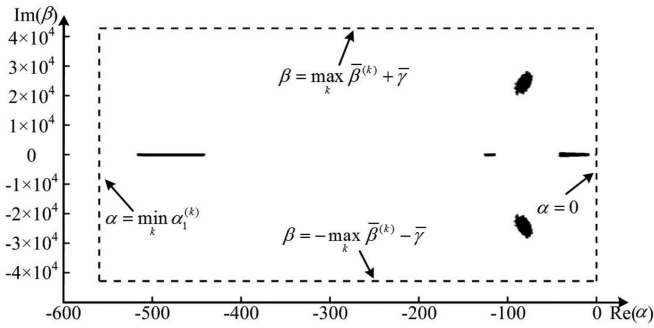
Fig. 6. Monte Carlo eigenvalue test results of a 100-machine system.

TABLE I
HARDWARE UTILIZATION OF THE MULTIDOMAIN MULTIMACHINE MODEL

Resource	LUT	FF	BRAM	DSP
Utilization	1021656 (86.42%)	433812 (18.34%)	92.5 (4.29%)	6286 (91.95%)

affect the imaginary part bounds, not only because $\max_k \overline{\beta}^{(k)}$ may change, but also that $\overline{\gamma}$ is a function of module number N, as shown in (25).

It is worth mentioning that although the above analysis are based on the aforementioned assumptions, they are still valid when taking into account the load torque transients as doing so does not affect the fact that $\mathbf{A}_2$ is a bipartite matrix because these modules are linked by a common dc bus.

IV. REAL-TIME EMULATION VALIDATION

To validate the above eigenvalue analysis, a MEA on board multi-domain multi-machine model is developed and implemented on Xilinx Virtex xcvu9p FPGA core for real-time emulation. The system contains 100 machine drive modules and each can be configured to interface pneumatic, hydraulic, or mechanical loads. Since the whole system is expressed in state-space form and the eigenvalue bounds are identified, it is convenient to solve it numerically. This paper adopts the classical 4th order Runge–Kutta (RK4) method working at 1 μs time-step as the numerical solver. Because of the explicit nature of RK4, the computation can be conducted in fully parallel manner. That is, the update of every state variable is solely based on history state information, thus can be completed synchronously and independently [29], a mechanism that is highly suitable for parallel hardware emulation on FPGA.

The FPGA implementation is accomplished using VHDL language in Vivado software. The hardware resource utilization for a 100 machine multi-domain multi-machine system is summarized in Table I.

In the following case-study, a 100-minute flight is simulated in real-time, where the pneumatic, hydraulic, and mechanical aspect characteristics from E-ECS, EHSA, and EMA along with their corresponding electrical domain performance waveforms are exhibited. Its validity is also corroborated by an off-line
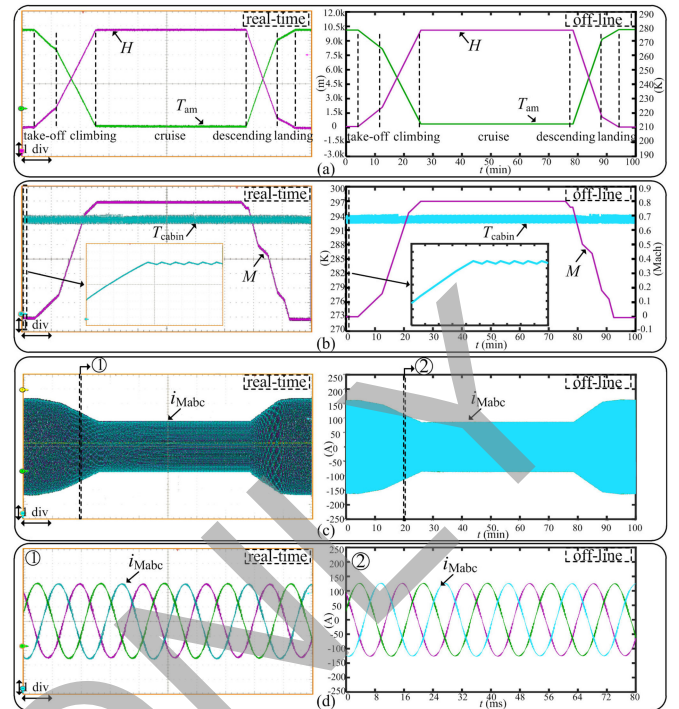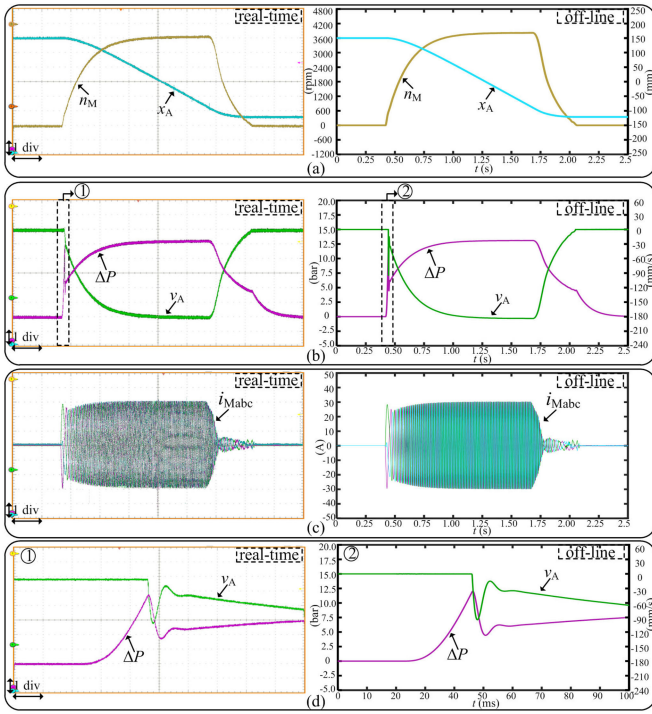

Fig. 7. Electric and pneumatic characteristics waveforms from E-ECS. (a) Aircraft altitude H: 1.5 km/div, atmosphere temperature T_{am}: 10 K/div, and time scale: 10 min/div. (b) Aircraft cabin temperature T_{cabin}: 3 K/div, aircraft speed (mach number) M: 0.1 Mach/div, and time scale: 10 min/div. (c) Three-phase machine currents i_{Mabc}: 50 A/div, and time scale: 10 min/div. (d) Magnified machine currents in the window shown in (c): i_{Mabc}: 50 A/div and time scale: 8 ms/div.

simulation of the same system performed at the same time-step on MATLAB/Simulink.

A. Electrical and Pneumatic Characteristics From E-ECS

Fig. 7 shows the performance waveforms from the E-ECS during the 100-minute flight. To make a comprehensive comparison, a complete mission profile including take-off, climbing, cruise, descending and landing phase is emulated and the corresponding aircraft altitude H and speed (mach numer) M, atmosphere temperature T_{am}, cabin temperature T_{cab} and machine currents i_{Mabc} waveforms are displayed in Fig. 7. As can be seen that, the cabin temperature remains almost constant (20 °C) once the E-ECS starts working. However, the atmosphere temperature changes with the flight mission (altitude) profile. As a result, the three-phase machine currents also changes. It is believed that the lower atmosphere temperature will reduce the pneumatic power required by the ECS because the cabin generally needs cooling rather than heating most of the flight time [30], which also coincides with the emulation outputs. To make a clear illustration, a short period of three-phase machine currents are also exhibited in Fig. 7. The real-time emulation results agree with the off-line results very well along the entire mission profile and less than 1% relative error is witnessed in all these quantities.

Fig. 8. Electric and hydraulic characteristics waveforms from EHSA. (a) Machine rotating speed n_M: 600 r/min/div, actuator position x_A: 50 mm/div, and time scale: 0.25 s/div. (b) Cylinder differential pressure $\triangle P$: 2.5 bar/div, actuator speed v_A: 30 mm/s/div, and time scale: 0.25 s/div. (c) Three-phase machine currents i_{Mabc}: 10 A/div and time scale: 0.25 s/div. (d) Magnified $\triangle P$ (2.5 bar/div) and v_A (30 mm/s/div) in the window shown in (b) and time scale: 10 ms/div.

B. Electrical and Hydraulic Characteristics From EHSA

Fig. 8 shows the response waveforms from EHSA when there is a step command on machine velocity from 0 to 3600 r/min at $t = 0.5$ s and back to 0 at $t = 1.5$ s. The machine rotating speed n_M, cylinder differential pressure $\triangle P$, actuator position x_A and speed v_A as well as machine currents i_{Mabc} are selected for observation during the simulation. Machine currents are stimulated during this period to generate electrical torque so as to push the hydraulic cylinder piston. Also, it can be observed that there is an obvious overshoot in the differential pressure and actuator speed when the system is initially started, which is a commonly witnessed feature in hydraulic system to overcome the static friction of the actuator rod [18]. The detailed transients of the overshoot are displayed in Fig. 8(d) to demonstrate the model's high fidelity. The relative error between real-time and off-line simulation is less than 1.2% even with the fast transients.

C. Electrical and Mechanical Characteristics From EMA

Fig. 9 shows the performance waveforms of EMA when the elevator moves from its initial position to the maximum extent angle at $t = 0.1$ s and swings back to the other direction at $t = 3.0$ s under the command. It is to be noted that there are multiple control loops in the system to meet the needs for flight control. Detailed description on the control scheme for EMA flight control can be found in [31]. The elevator position
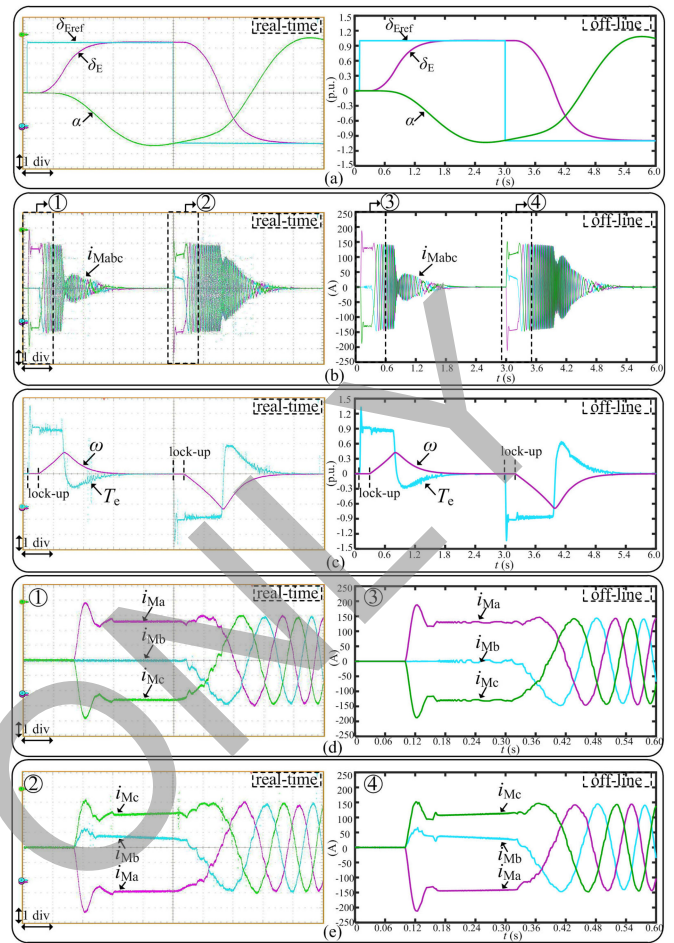
Fig. 9. Electric and mechanical characteristics waveforms from EMA. (a) Elevator position command $\delta_{E\mathrm{ref}}$, elevator response δ_E, and aircraft angle of attack α ($\tan\alpha = W/U$) response: 0.3 p.u./div and time scale: 0.6 s/div. (b) Three-phase machine currents i_{Mabc}: 50 A/div and time scale: 0.6 s/div. (c) Machine angular velocity ω and electrical torque T_e: 0.3 p.u./div and time scale: 0.6 s/div. (d) and (e) Magnified machine currents (50 A/div) in the window shown in (b) and time scale: 0.06 s/div.

command $\delta_{E\mathrm{ref}}$ and response δ_E, aircraft angle of attack α, machine currents i_{Mabc}, angular velocity ω and torque T_e are exhibited in Fig. 9. To guarantee safety, there is a brake system keeping the shaft standstill whenever the machine starts to move. It is until the electrical torque reaches certain value that the brake releases and the machine starts rotating. As a consequence, the three-phase current also keeps still during the lock-up period. This feature is also captured by the simulation. The relative error between real-time and off-line simulation results is slightly higher because of the sudden change in elevator position command and the multiple closed-loop control processes, but it is still less than 1.5%, which is acceptable in most engineering applications.

The above three test scenarios demonstrate that the real-time hardware model emulated on FPGA has the ability to accommodate multi-domain characteristics while in a multi-machine environment. The results match the off-line simulation results very well and could be a useful tool for hardware-in-the-loop test and design of MEA powertrains.

V. CONCLUSION

This article presented a modular assembly methodology for modeling the on-the-move MEA multi-domain multi-machine system. The featured pneumatic, hydraulic, and mechanical parts on MEA are modeled as modules and their mathematic descriptions were given. In addition, this article analyzed the eigenvalue bounds of the dc bus linked multi-machine drive system when assembling these modules. It was found that the real part eigenvalue bound of the assembled system does not grow with the module number. It was the maximum range of the real part bound among all these individual modules. However, the imaginary part bound always increased with the rise of module number. This article also gave practical eigenvalue bounds, both real and imaginary part, of the multi-machine drive system, which is useful when employing explicit numerical method to solve the system.

With the help of these theoretical analyses, real-time emulation of the power electronic based multi-domain multi-machine system on MEA was realized on FPGA. Pneumatic, hydraulic, and mechanical characteristics along with their related electrical performance waveforms were exhibited and compared with the off-line simulation results from commercial software. The emulation results from real-time model executed on FPGA hardware using RK4 solver were highly close to those obtained from off-line simulation, which validated the correctness of the theoretical analysis.

Electrical part parameters: dc bus voltage: ± 270 V; switching frequency of converter: 12 kHz; PMSM: stator winding resistance: 0.02 p.u., stator leakage reactance: 0.064 p.u., d- and q-axis reactance: 0.689 p.u., d-axis damper winding resistance: 0.055 p.u., d-axis damper reactance: 0.62 p.u., q-axis damper winding resistance: 0.183 p.u., d-axis damper reactance: 1.175 p.u., permanent magnet strength: 1.0 p.u.

Pneumatic part parameters: number of passengers: 290; compressor pressure ratio: 3.1; fan pressure ratio: 1.3; compressor and fan efficiency: 0.9; cooling mass flowing rate: 0.25 kg/s; air heat capacity ratio: 1.403; air heat capacity: 1003.5 J/kg·K; heat load per passenger: 110 W; fuselage heat conductivity: 1.4 W/m^2·K; solar radiation index: 0.3; solar radiation intensity: 250 W/m^2; fuselage area: 131 m^2.

Hydraulic part parameters: inertia on machine shaft: 2.865 $\times 10^{-3}$ kg·m^2; area of piston surface: 1.945 $\times 10^{-3}$ m^2; volumetric pump displacement: 9.05×10^{-7} m^3/rad; initial volume of chamber 1 and 2: 2.056 $\times 10^{-3}$ m^3; bulk modulus: 1.73 $\times 10^9$ kPa; leakage coefficient of the cylinder: 4.05 $\times 10^{-12}$ m^2/s·Pa; total mass of the piston rod: 16.52 kg; LuGre parameters for machine shaft: A_c: 0.8; B_c: 0.018; C_c: 0.8; z_c: 0.1; LuGre parameters for cylinder rod: A_c: 854; B_c: 9186; C_c: 5933; z_c: 2 $\times 10^{-4}$;

Mechanical part parameters: aircraft cruise speed: 890 ft/s; aircraft altitude: 35 000 ft; aircraft mass: 184 000 lbs; other parameters can be found in [23].

REFERENCES

[1] Y. Zhang *et al.*, "An energy efficient power management solution for a fault-tolerant more electric engine/aircraft," *IEEE Trans. Ind. Electron.*, vol. 66, no. 7, pp. 5663–5675, Jul. 2019.

[2] B. Li *et al.* "Modeling and simulation of aircraft power supply system based on Dymola and Modelica," in *Proc. Int. Conf. Electron. Syst. Aircr., Railway, Ship Propulsion Road Veh. Int. Transp. Electrific. Conf.*, 2016, pp 1–6.

[3] J. Batteh *et al.*, "Development and implementation of a flexible model architecture for hybrid-electric aircraft," in *Proc. 1st Amer. Modelica Conf.*, 2018, pp. 37–45.

[4] N. Cimmino *et al.*, "A modelling and simulation framework for the integrated design of aircraft systems," in *Proc. 7th Eur. Conf. Aeronaut. Aerosp. Sci.*, 2017.

[5] F. Schettini, E. Denti, and G. Di Rito, "Development of a simulation platform of all-electric aircraft on-board systems for energy management studies," *Aeronaut. J.*, vol. 121, no. 1239, pp. 710–719, May 2017.

[6] B. Yang, X. Wu, and W. Li, "FMI based multi-domain modeling and simulation for aircraft power distribution system," in *Proc. IEEE/CSAA Int. Conf. Aircr. Utility Syst.*, 2016, pp. 325–330.

[7] P. C. Krause, O. Wasynczuk, and S. D. Sudhoff, *Analysis of Electric Machinery and Drive Systems*. Piscataway, NJ, USA: Wiley–IEEE Press, 2002.

[8] O. Kahouli, M. Jebali, B. Alshammari, and H. H. Abdallah, "PSS design for damping low-frequency oscillations in a multi-machine power system with penetration of renewable power generations," *IET Renewable Power Gener.*, vol. 13, no. 1, pp. 116–127, Jan. 2019.

[9] M. J. Morshed and A. Fekih, "A coordinated controller design for DFIG-based multi-machine power systems," *IEEE Syst. J.*, vol. 12, no. 2, pp. 3211–3222, Sep. 2019.

[10] T. Yang, S. Bozhko, J. Le-Peuvedic, G. Asher, and C. I. Hill, "Dynamic phasor modeling of multi-generator variable frequency electrical power systems," *IEEE Trans. Power Syst.*, vol. 31, no. 1, pp. 563–571, Jan. 2016.

[11] Z. Shuai, Y. Peng, J. M. Guerrero, Y. Li, and Z. J. Shen, "Transient response analysis of inverter-based microgrids under unbalanced conditions using a dynamic phasor model," *IEEE Trans. Ind. Electron.*, vol. 66, no. 4, pp. 2868–2879, Jul. 2019.

[12] L. Wang *et al.*, "Methods of interfacing rotating machine models in transient simulation programs," *IEEE Trans. Power Del.*, vol. 25, no. 2, pp. 891–903, Apr. 2010.

[13] J. E. McNamara, "Electrically driven environmental control system," *IEEE Trans. Aerosp. Electron. Syst.*, vol. AES-20, no. 3, pp. 257–260, May 1984.

[14] A. Smith, T. Childs, and R. Chen, "Study into electrically shaft driven air cycle machines," in *Proc. 1st Int. Conf. Adv. Aerosp. Struct., Syst. Tech.*, 2018, pp 1–9.

[15] R. V. Díaz, "Analysis of an electric environmental control system to reduce the energy consumption of fixed-wing and rotary-wing aircraft," M.S. thesis, School Eng., Cranfield Univ., Cranfield, U.K., 2011. [Online]. Available: https://dspace.lib.cranfield.ac.uk/handle/1826/7422, Accessed on: Oct. 14, 2019

[16] H. Devadurgam, S. Rajagopal, and R. C. Munjulury, "Analytical design and estimation of conventional and electrical aircraft environmental control systems," *engrXiv*, vol. 11, Mar. 2019.

[17] S. Habibi and A. Goldenberg, "Design of a new high-performance electrohydraulic actuator," *IEEE/ASME Trans. Mechatronics*, vol. 5, no. 2, pp. 158–164, Jun. 2000.

[18] D. Belloli, F. Previdi, S. M. Savaresi, A. Cologni, and M. Zappella, "Modeling and identification of an electro-hydrostatic actuator," in *Proc. 5th IFAC Symp. Mechatronic Syst.*, 2010, pp. 620–625.

[19] K. J. Åström and C. Canudas-de-Wit, "Revisiting the LuGre friction model," *IEEE Control Syst. Mag.*, vol. 28, no. 6, pp. 101–114, Dec. 2008.

[20] M. Mazzoleni *et al.*, "Development of a reliable electro-mechanical actuator for primary control surfaces in small aircrafts," in *Proc. IEEE Int. Conf. Adv. Intell. Mechatronics*, 2017, pp. 1142–1147.

[21] D. McLean, *Automatic Flight Control Systems*. Englewood Cliffs, NJ, USA: Prentice-Hall, 1990.

[22] Z. Huang, C. Tang, and V. Dinavahi, "Unified solver based real-time multi-domain simulation of aircraft electro-mechanical-actuator," *IEEE Trans. Energy Convers.*, vol. 34, no. 4, pp. 2148–2157, Dec. 2019.

[23] T. I. Fossen, *"Mathematic Models for Control of Aircraft and Satellites,"* 3rd ed. Trondheim, Norway: Norwegian Univ. Sci. Technol., 2013.

[24] E. Ganev, "Selecting the best electric machines for electrical power-generation systems: High-performance solutions for aerospace More electric architectures," *IEEE Electrific. Mag.*, vol. 2, no. 4, pp. 13–22, Dec. 2014.

[25] C. A. Eschenbach and C. R. Johnson, "Sign patterns that require real, non-real or pure imaginary eigenvalues," *Linear Multilinear Algebra*, vol. 29, pp. 299–311, 1991.

[26] H. Wielandt, "On the eigenvalues of $\mathbf{A} + \mathbf{B}$ and $\mathbf{AB}$," *J. Res. Nat. Bureau Standards—B. Math. Sci.*, vol. 77B, no. 1/2, pp. 61–63, Jan.–Jun. 1972.

[27] P. F. Zachlin and M. E. Hochstenbach, "On the numerical range of a matrix," *Linear Multilinear Algebra*, vol. 56, no. 1/2, pp. 185–225, 2008.

[28] H. WoIkowicz and G. P. H. Styan, "Bounds for eigenvalues using traces," *Linear Algebra Appl.*, vol. 29, pp. 471–506, 1980.

[29] W. H. Press, S. A. Teukolsky, W. T. Vetterling, and B. P. Flannery, *Numerical Recipes: The Art of Scientific Computing*, 3rd ed. Cambridge U.K.: Cambridge Univ. Press, 2007.

[30] A. Pollok, "Modelling and control of aircraft environmental control systems," Ph.D. dissertation, Dept. Elect. Inf. Bioingegneria, Polytech. Univ. Milan, Milan, Italy, 2017. [Online]. Available: https://elib.dlr.de/119309/1/thesis.pdf, Accessed on: Oct. 14, 2019

[31] A. Trentin, P. Zanchetta, P. Wheeler, and J. Clare, "Power flow analysis in electro-mechanical actuators for civil aircraft," *IET Elect. Power Appl.*, vol. 5, no. 1, pp. 48–58, Jan. 2011.

Chengcheng Tang (Student Member, IEEE) received the B.S. degree in electrical engineering from North China Electric Power University, Baoding, China, in 2013 and the M.Eng. degree in biomedical engineering from Tsinghua University, Beijing, China, in 2018. She is currently pursuing her Ph.D. degree in electrical engineering with the Department of Electrical and Computer Engineering, University of Alberta, Edmonton, Canada.

Her current research interests include modeling and simulation of more electric aircraft.

Zhen Huang (Student Member, IEEE) received the B.S. degree from Xi'an Jiaotong University, Xi'an, China, in 2012 and the M.S. degree from Tsinghua University, Beijing, China, in 2015, both in electrical engineering. He is currently pursuing his Ph.D. degree in electrical engineering with the Department of Electrical and Computer Engineering, University of Alberta, Edmonton, Canada.

He also has two years work experience in power Electronic industry. His current research interests include high-performance simulation and control of power electronics and power systems.
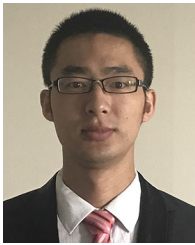
Tong Duan (Student Member, IEEE) received the B.S. degree in electronic engineering from Tsinghua University, Beijing, China, in 2013, and he is currently pursuing the Ph.D. degree in electrical and computer engineering at the University of Alberta, Edmonton, Alberta, Canada.

His current research interests include real-time simulation of power systems, communication networking, and field-programmable gate arrays.

Venkata Dinavahi (Fellow, IEEE) received the B.Eng. degree from Visvesvaraya National Institute of Technology, Nagpur, India, in 1993, the M.Tech degree from the Indian Institute of Technology, Kanpur, India, in 1996, both in electrical engineering, and the Ph.D. degree in electrical and computer engineering from the University of Toronto, Toronto, ON, Canada, in 2000.

He is currently a Professor with the Department of Electrical and Computer Engineering, University of Alberta, Edmonton, AB, Canada. His current research interests include real-time simulation of power systems and power electronic systems, electromagnetic transients, device-level modeling, large-scale systems, and parallel and distributed computing.